JGR Planets

RESEARCH ARTICLE
10.1029/2020JE006451

Key Points:
- We carry out numerical and theoretical analysis of an idealized model of tidallydriven hydrothermalactivity inside Enceladus
- With numerical and theoretical analysis, we explore the flow that develops in a porous core with volumetric heating
- Our model allows us to predict typical temperature, velocity, and heat-flux anomalies at the bottom of Enceladus' subsurface ocean

Correspondence to:
T. Le Reun,
tl402@cam.ac.uk

Citation:
Le Reun, T., & Hewitt, D. R. (2020). Internally heated porous convection: An idealized model for Enceladus' hydrothermal activity. *Journal of Geophysical Research: Planets*, *125*, e2020JE006451. https://doi.org/10.1029/2020JE006451

Received 12 MAR 2020
Accepted 19 JUN 2020
Accepted article online 26 JUN 2020

©2020. The Authors.
This is an open access article under the terms of the Creative Commons Attribution License, which permits use, distribution and reproduction in any medium, provided the original work is properly cited.

Internally Heated Porous Convection: An Idealized Model for Enceladus' Hydrothermal Activity

Thomas Le Reun[1] and **Duncan R. Hewitt**[2]

[1]DAMTP, University of Cambridge, Cambridge, UK, [2]Department of Mathematics, University College London, London, UK

Abstract Recent planetary data and geophysical modeling suggest that hydrothermal activity is ongoing under the ice crust of Enceladus, one of Saturn's moons. According to these models, hydrothermal flow in the porous, rocky core of the satellite is driven by tidal deformation that induces dissipation and volumetric internal heating. Despite the effort in the modeling of Enceladus' interior, systematic understanding—and even basic scaling laws—of internally heated porous convection and hydrothermal activity are still lacking. In this article, using an idealized model of an internally heated porous medium, we explore numerically and theoretically the flows that develop close to and far from the onset of convection. In particular, we quantify heat-transport efficiency by convective flows as well as the typical extent and intensity of heat flux anomalies created at the top of the porous layer. With our idealized model, we derive simple and general laws governing the temperature and hydrothermal velocity that can be driven in the oceans of icy moons. In the future, these laws could help better constraining models of the interior of Enceladus and other icy satellites.

Plain Language Summary Enceladus, one of Saturn's icy moons, is known from planetary data to be the site of ongoing hydrothermal activity. According to recent modeling, this activity is driven by tidal distortion throughout its porous rocky core, which causes friction and induces volumetric heating. As subsurface liquid water penetrates through the core, it warms, rises, and returns into the ocean through localized hot spots. We introduce an idealized model of this hydrothermal circulation in order to understand the formation of hot spots, their typical size, and their activity. We find that the hydrothermal flow in the porous core of Enceladus is about a few centimeters per year and is thus much slower than circulations in the Earth's ocean crust. As a result, the timescale for hot-spot activity-variations is as long as a few million years. Despite the slowness of the circulation, we predict that it drives oceanic plumes with velocity of the order of 1 $cm \cdot s^{-1}$.

1. Introduction

Enceladus, a 500 km diameter icy satellite orbiting Saturn, has drawn a lot of attention since the first flybys operated by the Cassini probe in 2005. Pictures and in situ astrochemical measurement have revealed the presence of a water vapor and ice plume ejected into outer space. It emerges along fractures in the ice crust at the south pole of Enceladus and is associated with a large heat-flux anomaly of 12.5 GW (Spencer et al., 2006, 2018). Subsequent analyses have revealed that the ejected material contains silicate particles of nanometric size whose chemistry indicates that the water contained in the plume has been previously hot, liquid, and in contact with silicate rocks (Hsu et al., 2015; Sekine et al., 2015). Enceladus' plumes have since then been interpreted as evidence for hydrothermal activity occurring below the ice crust of Enceladus. This is a surprising implication because, unlike the Earth, Enceladus has radiated away all its initial heat, and its small size makes internal heating by radiogenic elements insufficient to explain the abnormal heat flux (Choblet et al., 2017; Nimmo & Pappalardo, 2016).

Building on the recent study of Lainey et al. (2017), Choblet et al. (2017) have recently proposed a self-consistent model to explain the hydrothermal activity based on internal heating by tides in Enceladus' water-saturated porous core. This model relies on recent findings regarding the interior of Enceladus. Underneath its ice crust, this satellite comprises a global subsurface ocean, with thickness varying from 30 to 50 km (Thomas et al., 2016). Below lies a core made of rocky material that remains undifferentiated and uncompacted owing to to the weakness of Enceladus' gravity field (Choblet et al., 2017; Roberts,

2015). The core is thus permeated with the water of the ocean; Choblet et al. (2017) estimate that the porosity ranges from 20% to 30% for a water-filled rocky core. Lastly, intense internal heating (Lainey et al., 2017) due to tidally induced deformation and friction heats the water and creates a porous flow with hot and narrow upwelling zones, possibly leading to hot spots of water flowing into the ocean (Choblet et al., 2017).

Hydrothermal convection with internal heating is only a relatively recent feature of thermal evolution models (Travis & Schubert, 2015; Travis et al., 2012), and it is in general driven by radiogenic heating or serpentinization rather than tidal deformation (Nimmo & Pappalardo, 2016). However, interior models of icy moons deal with very poorly constrained parameters; for instance, the permeability of the core, for which a range of orders of magnitudes is plausible (Choblet et al., 2017; Travis & Schubert, 2015). Despite systematic studies covering a wide range of parameters (Choblet et al., 2017), general scaling laws predicting the size and intensity of heat-flux anomalies, the typical temperature or hydrothermal velocity and their dependence on physical parameters are still lacking. By investigating a basic model for internallyheated porous convection, we aim to derive these scaling laws, which could prove useful to better constrain the planetary data available for Enceladus or to build thermal evolution models of icy moons more generally (Travis & Schubert, 2015; Travis et al., 2012).

In the present article, we thus explore systematically internallyheated porous convection close to and far from the onset of motion with numerical simulations and mathematical analysis. We use an idealized two-dimensional Cartesian model of a water-saturated porous layer with internal heating in order to reduce the complexity of the system as much as possible while retaining the key physical ingredients, which are internal heating and an open-top boundary. This kind of approach has a long history of use in convection studies. The canonical model to study heat transport by convection is the Rayleigh-Bénard setup (a confined porous layer heated from below and cooled from the top) which has received a significant amount of study (Hewitt & Lister, 2017; Hewitt et al., 2012, 2014; Otero et al., 2004). The more closely related case of Earth-like hydrothermal systems with a bottom heat flux and open-top boundary has also been widely studied (see, for instance, Coumou et al., 2008, 2009; Fontaine & Wilcock, 2007). However, the results of these investigations are unlikely to apply to tidally driven hydrothermal circulation because of either unsuitable boundary condition or the nature of the heat source. Very few systematic experimental and numerical studies have been devoted to internally heated porous convection. Those that have are focused mostly on the onset of motion and average heat transport (Buretta & Berman, 1976; Hardee & Nilson, 1977; Kulacki & Ramchandani, 1975; Nield & Kuznetsov, 2013). Hence, these studies do not allow the derivation of scalings governing, for instance, the typical extent of upwelling zones or the associated thermal anomalies and fluid velocities, in the case of tidally driven hydrothermal activity. That is our aim here.

In common with numerous convection setups, we find that the intensity of heat-transporting motion is characterized by only one dimensionless number, the Rayleigh number, noted Ra, which increases with volumetric heat production, permeability, and core radius. Performing numerical simulations and asymptotic analysis, we find that the typical size of thermal anomalies is proportional to $Ra^{-1/2}$, owing to a balance between advection, heat production, and advection. As a consequence, the plumes driven in the ocean by thermal anomalies have a buoyancy flux scaling like $Ra^{3/2}$. When quantified for ranges of parameters that are expected for Enceladus, we predict typical Darcy fluxes in the core of at most 10 cm·yr^{-1}, while hydrothermal velocities are expected to reach about 1 cm·s^{-1}.

This paper is organized as follows. The first part is devoted to introducing our idealized model for an internally heated, saturated porous layer, and identifying the relevant dimensionless parameters. We then carry out a stability analysis to determine the conditions under which convection happens. Afterward, we describe and analyze numerical simulations of internally-heated porous convection, focusing in particular on the structure of the flow and the associated thermal anomalies. Lastly, we apply the laws derived from our idealized model to Enceladus to quantify the temperature anomalies and the typical hydrothermal velocities that can be induced in its ocean.

2. A Simple Model for the Interior of Icy Moons

2.1. The Model and Its Governing Equations

We consider an idealized model of tidally driven convection inside icy moons of the type of Enceladus to focus on the effect of two fundamental ingredients: internal heating and an open-top boundary. We thus

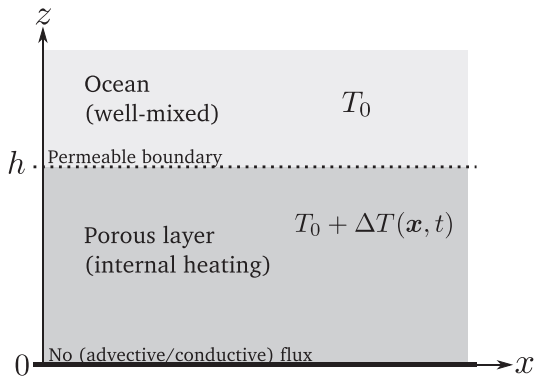

Figure 1. An idealized two-dimensional model to describe porous convection inside core in interaction with the subsurface ocean in an icy moon of the type of Enceladus. The bottom of the porous layer models the center of the moon; there is no heat and mass flux at this height. Mass exchange between the ocean and the porous core are allowed with a free vertical velocity at the top.

make a series of simplifying approximations. First, rather than modeling the full fluid system, comprising the water-saturated core and the ocean, we consider only the core, and we parametrize the core-ocean interaction via boundary conditions that will be specified below. Second, we consider a two-dimensional Cartesian model instead of modeling a full sphere. Third, we treat the gravitational field as constant in space, although it should increase away from the center of the moon, and we consider either constant or horizontally varying internal heat generation, although it, too, should vary with depth. We treat all other parameters, including the permeability, as constants. We will return in section 6 to consider and discuss the effect of some of these assumptions, as we apply our general findings and scalings to the case of Enceladus.

We thus consider a two-dimensional porous core of (uniform) permeability k, which is saturated with water of viscosity μ. It lies beneath an ocean that we assume to be well mixed with a global temperature T_0 (see Figure 1). The volume (or Darcy) flux $\boldsymbol{U}=(U,W)$ inside the porous core is modeled by Darcy's law,

$$\boldsymbol{U} = \frac{k}{\mu}(-\nabla P + \rho \boldsymbol{g}), \tag{1}$$

where P is the pressure, ρ is the density of water, and $\boldsymbol{g}$ is the gravity field, pointing in the z direction. Note the the volume flux $\boldsymbol{U}$ is related to the fluid velocity $\boldsymbol{U}_f$ by the porosity φ of the matrix such that $\boldsymbol{U}=\varphi \boldsymbol{U}_f$. In addition to Darcy's law, the flow is assumed to be incompressible, so that the volume flux must also satisfy a continuity equation,

$$\partial_x U + \partial_z W = 0. \tag{2}$$

Water motion inside the core is driven by buoyancy and temperature differences. We model the effects of temperature on density assuming linear expansion of the fluid with temperature under the Boussinesq approximation, such that $\rho = \rho_0(1-\alpha(T-T_0))$ where ρ_0 is a reference density and α the thermal expansion coefficient. Darcy's law may thus be written as

$$\boldsymbol{U} = \frac{k}{\mu}\left(-\nabla P' + \rho_0 g \alpha \Theta \boldsymbol{e}_z\right), \tag{3}$$

where $P' = P+\rho_0 g z$ and $\Theta \equiv T - T_0$. Since the flow is driven by thermal anomalies Θ, we must introduce an equation modeling the transport of heat inside the porous medium. This is achieved using thermal energy conservation, in which a source term accounting for volume heat production is included (Nield & Bejan, 2013; Souček et al., 2014):

$$\overline{\varphi}\ \partial_t \Theta + \boldsymbol{U} \cdot \nabla \Theta = \kappa \nabla^2 \Theta + q, \tag{4}$$

with κ the volume-averaged heat diffusivity inside the porous medium (i.e., of both water and the porous matrix together), $\overline{\varphi}$ a modified porosity and q is the internal heat source term. Under the assumption of local thermal equilibrium between the fluid and the matrix, the modified porosity $\overline{\varphi}$ and the volume-averaged diffusivity are combinations of the porosity, φ, the heat capacity per unit of mass of the matrix and water, c_m and c_0, and the density of the matrix and water, ρ_m and ρ_c, such that

$$\overline{\varphi} = \frac{(1-\varphi)\rho_m c_m + \varphi \rho_0 c_0}{\rho_0 c_0} \quad \text{and} \quad \kappa = \frac{(1-\varphi)\lambda_m + \varphi \lambda_0}{\rho_0 c_0} \tag{5}$$

(Nield & Bejan, 2013; Souček et al., 2014), where the $\lambda_{m,0}$ are the heat conductivity of the matrix and water. The source term q is related to the volumetric heat production by tidal heating Q_V via $q=Q_V/(\rho_0 c_0)$. In this

paper, we consider two idealized limits: Either Q_V is constant, or it is assumed to vary laterally (i.e., in x) to model tidal heating inhomogeneities.

2.2. Boundary Conditions

Throughout this work, we impose periodic boundary conditions in the horizontal direction. The bottom of the porous layer roughly corresponds to the core center, and so we assume that there is no heat or mass flux crossing the bottom boundary, that is,

$$\partial_z \Theta(z=0) = 0 \quad \text{and} \quad W(z=0) = 0. \tag{6}$$

The top of the layer at $z=h$ is in contact with the ocean and must allow mass exchange between the core and the ocean. This is achieved by imposing a purely vertical velocity at the top, that is,

$$U(z=h) = 0. \tag{7}$$

The two layers are also thermally coupled, and we consider two possible boundary conditions for θ on the upper boundary. One first natural choice is to impose the temperature (on the upper boundary) to be the temperature of the ocean, that is,

$$\Theta(z=h) = 0. \tag{8}$$

However, in this case, the advective heat flux driving hydrothermal activity $W\Theta(z=h)$ across the interface would vanish, which seems at odds with the idea that the water coming out the porous layer may drive a buoyant plume rising in the ocean. We could alternatively use another boundary condition where the temperature of water is left unchanged as it leaves the porous layer, while water enters with the imposed temperature of the ocean, that is,

$$\begin{cases} \partial_z \Theta(z=h) = 1 & \text{if } W > 0 \\ \Theta(z=h) = 0 & \text{else.} \end{cases} \tag{9}$$

Such a boundary condition is a standard parametrization of core-ocean interactions (Choblet et al., 2017; Cserepes & Lenkey, 2004; Monnereau & Dubuffet, 2002; Rabinowicz et al., 1998).

The thermal boundary conditions (8) and (9) may be regarded as two end-members of the fully coupled problem of the core-ocean interaction. In the case of slow ascent in the porous medium, diffusion from the ocean inside the core causes the temperature inside the porous medium to drop in the top boundary vicinity. Conversely, if the upwelling is fast, diffusion is not able to affect the temperature inside the ascending plume. As a side note, intermediary situations where $\partial_z \Theta(z=h) = -\beta$ with $\beta>0$ could also be considered. Nevertheless, choosing between the two boundary conditions or parametrization of β would require a demanding study of the fully coupled system involving both the ocean and the porous core. We instead carry out two sets of simulations using either boundary conditions (8) and (9). We will find that the choice of boundary condition does not significantly affect the flow in the interior of the core.

2.3. Scaling the Problem: Dimensionless Equations

First, all considered lengths are normalized by the height of the porous layer h. We must also define volume flux and temperature scales, respectively denoted as U^* and Θ^*. Darcy's law (3) gives a simple relation between these two scales,

$$U^* = \frac{k}{\mu} \rho_0 \alpha g \Theta^*. \tag{10}$$

Unlike in, say, a Rayleigh-Bénard setup, the temperature scale Θ^* is not naturally imposed in the internally heated problem. We predict that in the nonlinear regime, heat production and advection will be the dominant balance in Equation 4, leading to the following relation between the velocity and temperature scales,

$$U^*\Theta^* = hq. \tag{11}$$

Both scales then can be written as a function of physical parameters as follows:

$$U^{*2} = \frac{k}{\mu}\rho_0 \alpha g h q \quad \text{and} \quad \Theta^* = \sqrt{\frac{\mu h q}{k \rho_0 \alpha g}} \tag{12}$$

Given these scales, we find that the system is governed by only one dimensionless parameter, a Rayleigh number comparing the relative importance of advection and diffusion,

$$Ra \equiv \frac{hU^*}{\kappa} = \left(\frac{k\alpha g}{\kappa \nu}\frac{qh^2}{\kappa}h\right)^{1/2}. \tag{13}$$

Note that other definitions have been considered for the Rayleigh number, depending in particular on the expected balance at play. For instance, Buretta and Berman (1976) choose volume flux and temperature scales based on an advection and diffusion balance, rather than a balance between advection and heat production considered in Equation 11, leading to a Rayleigh number Ra_{bb}=Ra^2.

Introducing the dimensionless temperature $\theta = \Theta/\Theta^*$ and volume flux $\boldsymbol{u} = \boldsymbol{U}/U^*$, the dimensionless governing equations for a porous layer with internal heating are

$$\begin{cases} \nabla \cdot \boldsymbol{u} &= 0 \\ \boldsymbol{u} &= -\nabla p + \theta \boldsymbol{e}_z \\ \partial_t \theta + \boldsymbol{u} \cdot \nabla \theta &= \dfrac{1}{Ra}\nabla^2 \theta + 1, \end{cases} \tag{14}$$

where time is normalized by $\overline{\varphi}h/U^*$ and pressure is rescaled by $\mu U^*/(hk)$. The flow being incompressible and two-dimensional, it is convenient to introduce a stream function ψ such that $\boldsymbol{u} = \nabla\times(-\psi \boldsymbol{e}_y)$. The governing Equations 14 become

$$\begin{cases} \nabla^2 \psi &= -\partial_x \theta \\ \partial_t \theta + \partial_z \psi \partial_x \theta - \partial_x \psi \partial_z \theta &= \dfrac{1}{Ra}\nabla^2 \theta + 1. \end{cases} \tag{15}$$

Lastly, the vertical boundary conditions are

$$w(z=0) = u(z=1) = \partial_z \theta(z=0) = 0, \tag{16}$$

and either

$$\text{BC } 1 : \theta(z=1) = 0, \ \text{ or} \tag{17}$$

$$\text{BC } 2 : \begin{cases} \partial_z \theta(z=1) = 1 \text{ if } w > 0, \\ \theta(z=1) = 0 \text{ else}, \end{cases} \tag{18}$$

for the temperature. Note that the boundary conditions on the volume flux translate into $\partial_z \psi(z=1)$=$\psi(z=0) = 0$. Lastly, the domain is periodic in the x direction.

2.4. Numerical Modeling

We study this problem numerically with the code developed by Hewitt et al. (2012). At each time step, Darcy's law is used to determine the stream function using Fourier transform in the horizontal direction and second-order finite differences in the vertical direction. The time evolution of the advection-diffusion equation is solved using an alternating direction implicit scheme (Press et al., 1992). The diffusion term is discretized using standard second-order accurate finite differences and the use of two staggered grids for the stream function ψ and the temperature field θ allows flux-conservative discretization of the advection term. The finite difference in time is second-order accurate as well. Anticipating strong gradients near the

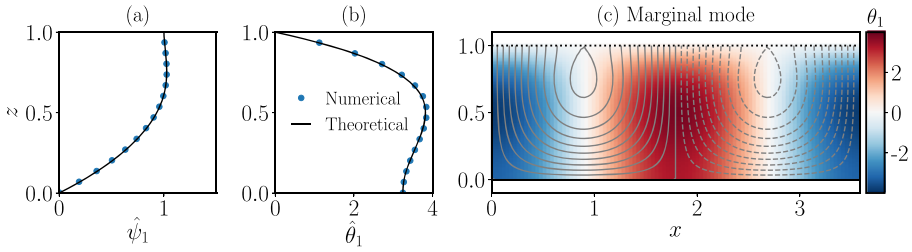

Figure 2. (a and b) Vertical structure functions of the stream function $\hat{\psi}_1$ and $\hat{\theta}_1$ of the marginal mode obtained by solving the boundary value problem (22) (black line) and extracted from a direct numerical simulation of the instability close to the threshold ($Ra-Ra_c \simeq 3\times10^{-2}$). (c) Temperature field (θ_1) and streamlines (isocontours of ψ_1) of the unstable mode at the onset of convection.

boundaries, a vertical stretched grid is implemented to ensure the boundary layers are well resolved. The numerical discretization of Equations 15 is tested in section 3.

3. The Onset of Convection

In this section, we investigate both theoretically and numerically the critical value of the Rayleigh number Ra above which a convective instability develops. The steady, purely diffusive base state ($\boldsymbol{u}=0,\theta_b$) on which the instability develops is

$$\theta_b(z) = \frac{Ra}{2}\left(1-z^2\right), \tag{19}$$

regardless of the upper thermal boundary condition. We look for perturbations to the base state of the form (Drazin, 2002)

$$\psi = \psi_1(\boldsymbol{x})e^{\sigma t} \qquad \text{and} \qquad \theta = \theta_b + \theta_1(\boldsymbol{x})e^{\sigma t}, \tag{20}$$

such that $|\psi_1|,|\theta_1| \ll \theta_b$. The exponential terms allow to account for the existence of a convective instability characterized by $\mathrm{Re}(\sigma) > 0$. Using the ansatz (20), Equations 15 to leading order in ψ_1, θ_1 yield the following single, fourth-order differential equation on the stream function:

$$\nabla^4\psi_1 = Ra\sigma\nabla^2\psi_1 - zRa^2\partial_{xx}\psi_1. \tag{21}$$

The invariance under translation along the x-axis allows further simplification by assuming that ψ_1 is a plane wave in x, that is $\psi_1 = \hat{\psi}_1(z)\exp(ikx)$. Equation 21 with the plane wave assumption yields the following ordinary differential equation for the function $\hat{\psi}_1$:

$$\hat{\psi}_1'''' - (2k^2 + Ra\sigma)\hat{\psi}_1'' + (k^4 + Ra\sigma k^2 - zRa^2k^2)\hat{\psi}_1 = 0, \tag{22}$$

where σ is an unknown eigenvalue. We solve numerically the one-dimensional boundary value problem (22) using BC 1 in (17). (In fact, for this onset problem, BC 2 (18) gives an ill-posed system.) We find the lowest value of the Rayleigh number for which σ=0 to be $Ra=Ra_c\simeq5.894$ at $k=k_c\simeq1.751$. Such a value for the critical Rayleigh number is close to the value 5.72 found experimentally and theoretically by Buretta and Berman (1976) in a system with closed boundary conditions. The marginal mode and its vertical structure functions ($\hat{\psi}_1$ and $\hat{\theta}_1$) are shown in Figure 2. The mode comprises a half-roll structure, with strong horizontal flow at the lower boundary and strong vertical flow at the upper boundary. The temperature deviation is maximized roughly halfway up the roll.

We use this theoretical investigation of the onset of convection to benchmark the numerical code. Simulations were carried out at values of the Rayleigh number Ra very close to the onset ($|Ra-Ra_c| \leq 10^{-1}$ typically). The horizontal extent of the domain is chosen to match approximately twice the wave length of the marginal mode. Computations were initiated with a small perturbation to the diffusive temperature

Table 1
Numerical Simulations Carried Out Indicating the Nature of the Boundary Condition, the Aspect Ratio of the Domain, the Range of Rayleigh Numbers, and the Associated Horizontal (n_x) and Vertical (n_z) Resolutions

Boundary conditions	Aspect ratio L	Rayleigh number range	Resolution ($n_x \times n_z$)
BC 1, 2	4	6-20	128×300
		20–100	256×300
		100–770	512×400
		550–2,000	1,024×500
		3,000–10,000	2,048×500
BC 2	3	6-20	128×300
		20–100	256×300
		100–770	512×400
		550–2,000	1,024×500
		3,000–10,000	2,048×500
BC 2	8	6-20	256×300
		20–100	512×300
		100–770	1,024×400
		550–3,000	2,048×500

Note. Note that the resolution is increased close to the boundaries by the use of a stretched vertical grid.

profile (19). We observed an exponential growth or decay of the amplitude of the perturbation to the diffusive base state and found accurate reproduction of both the critical Rayleigh number and the growth or decay rate of the most unstable mode for nearby values of *Ra*. Figure 2 shows the excellent agreement between the theoretical and the computed vertical structure functions $\hat{\theta}_1$ and $\hat{\psi}_1$.

4. Nonlinear Heat Transport by Convection

In the following section, we investigate heat transport by convection for larger values of *Ra*. We first describe qualitatively the organization of the flow as *Ra* is increased. We then show quantitatively that nonlinear heat transport is dominated by advection, which constrains the typical size of hot plumes and thermal anomalies. We use both thermal boundary conditions (17) and (18) to find that the difference between them is negligible for large enough values of *Ra*.

4.1. Numerical Process

Prior to delving into the results of the simulations, we explain how a typical numerical simulation is carried out. The simulations are initialized with random noise at a certain Rayleigh number *Ra*. After the initial growth of the instability, the flow reaches a statistically steady state. It is assessed by computing at each time step the mean of the maximum temperature since the start of the simulation: Such a cumulative average converges toward a constant once the statistically steady state is reached. The simulation is terminated once the steady state has lasted for 300 time units. The Rayleigh number is then switched to a new value, and the simulations is initiated with the last state of the previous one plus a small noise disturbance. A summary of all the numerical simulations that have been carried out is given in Table 1.

4.2. Flow Structures and Organization

To introduce the nonlinear behavior of the instability driven by internal heating, we first illustrate typical flow patterns observed at different Rayleigh numbers. Figure 3 displays typical snapshots of the temperature field. At low Rayleigh number, that is, for $Ra_c \leq Ra < 20$, the convection reaches a steady state with few plumes, be it for boundary condition BC 1 or BC 2 (see Figure 3a). Similar to the unstable mode at threshold, these plumes consist of half rolls, although with steeper vertical gradients at the top boundary in the case of BC 1. For larger Rayleigh numbers (see Figure 3b), the flow exhibits an unsteady chaotic behavior where usually two modes with different number of plumes alternate, thus inducing chaotic merging and growth of plumes. This situation ceases at $Ra \simeq 600$, at least for an aspect ratio $L=4$: higher values of the Rayleigh number give rise to steady solutions with a large number of narrow plumes (see Figure 3c).

The only noticeable difference between the two boundary conditions is the existence of a thin thermal boundary layer when the top temperature is imposed (BC 1). Its thickness, of order Ra^{-1}, is set by a balance

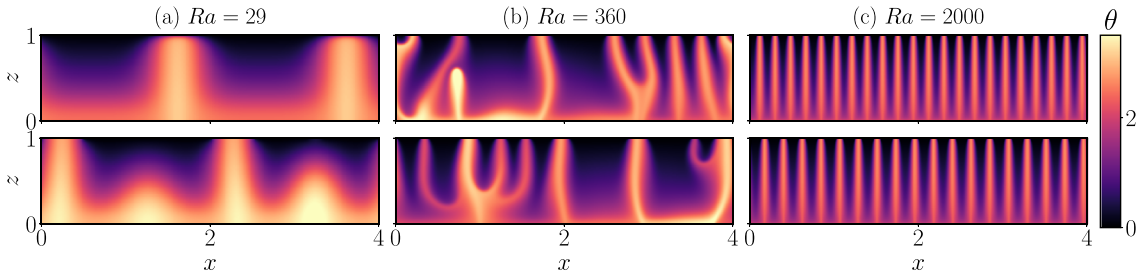

Figure 3. Snapshots of the temperature field θ at *Ra*=29 (a), 360 (b), and 2,000 (c) for boundary condition BC 1 (top) and BC 2 (bottom), taken once a statistically steady state is reached. The flow exhibits chaotic behavior for the two lowest values of the Rayleigh number and is steady at *Ra*=2,000. Apart from the thin top boundary layer, both boundary conditions (17) and (18) overall produce the same flow. The difference in the plume number at *Ra*=2,000 between the two boundary conditions is rather due to the simultaneous stability of different modes.

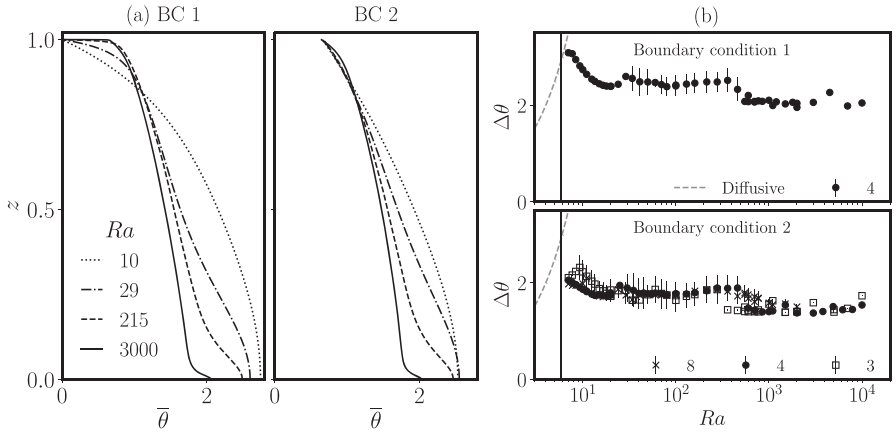

Figure 4. (a) Averaged temperature profiles $\overline{\theta}(z)$ for different Rayleigh numbers and both boundary conditions and aspect ratio $L = 4$. At large Ra, the profiles given by BC 1 and BC 2 are strikingly similar apart from the upper boundary layer for BC 1. Note the emergence of a thermal boundary layer at $z = 0$ where the heat that is produced locally is carried away through diffusion only. Although it creates sharp variations, the bottom boundary condition $\overline{\theta}'(0) = 0$ remains satisfied even when rapid variations are observed at $Ra = 3{,}000$. (b) Mean temperature difference between the bottom and the top of the porous layer Θ^* as a function of the Rayleigh number Ra, for all simulations carried out with BC 1 (top) and BC 2 (bottom), and different values of aspect ratio L as marked. The error bars correspond to the standard deviation over time of the average temperature difference. The diffusive temperature difference $\Delta\theta = Ra/2$ is shown for comparison (dashed line). The vertical line marks the critical Rayleigh number Ra_c.

between vertical advection and diffusion. In addition, the high degree of similarity between the simulations carried out with different boundary condition suggests that the mixed boundary condition (BC 2) is reliable. Note that this is not the case below the threshold of the instability where flows that are highly sensitive to initial condition are observed. We therefore choose to use both boundary conditions in the study detailed hereafter, as long as $Ra > Ra_c$. Lastly, note that in these snapshots $\theta = \mathcal{O}(1)$, which confirms that the balance between advection and heat production drives the dynamics, a balance that was foreseen in section 2.3.

4.3. Advective Heat Transport

The qualitative analysis of snapshots carried out in the preceding section indicates that advection dominates heat transport. We propose in the following a quantitative analysis of the flow to support this assertion, in

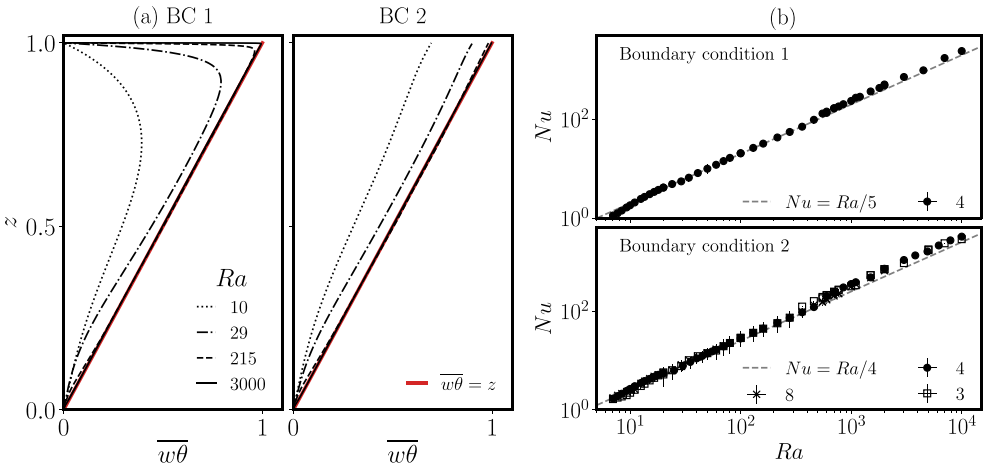

Figure 5. (a) Vertical variations of the horizontally averaged advective heat flux $\overline{w\theta}(z)$, for boundary condition BC 1 (left) and 2 (right) and aspect ratio $L = 4$. Again, we note the similarity between the two boundary conditions in the bulk of the porous medium. The asymptotic law $\overline{w\theta} = z$ (25) is given for reference. (b) Plot of the Nusselt number Nu as a function of the Rayleigh number Ra for all simulations carried out with boundary conditions BC 1 and 2 (top and bottom panels, respectively), and different values of aspect ratio L as marked. The error bars correspond to the standard deviation in time of the instantaneous Nusselt number $N(t)$ (see Equation 26).

particular of the vertical temperature and heat flux profiles. This analysis will allow us to compare internally heated porous convection with the more classical Rayleigh-Bénard problem via the introduction of a generalized Nusselt number.

4.3.1. The Mean Temperature Scale

It has been noted in the preceding section that the typical values of the temperature field remain of $O(1)$. To better quantify this observation, we introduce a dimensionless temperature scale $\Delta\theta = \overline{\theta}(z=1) - \overline{\theta}(z=0)$, where the operation $\overline{\cdot}$ denotes horizontal and temporal average in the statistically steady state. Typical profiles of the horizontally averaged temperature are shown in Figure 4a. The average temperature is a decreasing function of height that converges toward an asymptotic profile at high Rayleigh number. We note again the strong similarity between the two boundary conditions, especially at large Rayleigh numbers where they only differ by the presence of the top thermal boundary layer. The temperature scale $\Delta\theta$ is also plotted in Figure 4 as a function of the Rayleigh number for all simulations. We note it is well below the diffusive scaling $\Delta\theta \propto Ra$ even very close to the threshold of the instability. $\Delta\theta = O(1)$ is a signature of efficient transport and vertical mixing of the thermal energy by the convective flows. In addition, we note a marked decrease of $\Delta\theta$ at $Ra \simeq 600$, which corresponds to the transition from the chaotic to the steady regime. It indicates that the steady flow is even more efficient at transporting heat out of the system. Anomalous points may however be noticed; they are due to the locking of the simulation on a particular mode (i.e., a flow with a certain number of plumes) that remains stable as the Rayleigh number is slightly increased. We found that starting from a different initial condition at the same Rayleigh number can give steady states with a different number or plumes, which suggests that the past history of the system has some influence on its current state.

4.3.2. The Advective Flux

To further quantify heat transport in the strongly nonlinear regime, we consider here the vertical heat flux, defined as

$$J = w\,\theta - \frac{1}{Ra}\frac{\partial \theta}{\partial z}, \tag{23}$$

which comprises an advective and a diffusive contribution. Time-averaged thermal energy conservation (14) prescribes a balance between vertical heat transport and volumetric heat production such that

$$\frac{\mathrm{d}\overline{J}}{\mathrm{d}z} = 1, \quad \text{that is} \quad \overline{J}(z) = z. \tag{24}$$

In the asymptotic regime of high Rayleigh number, we expect that the heat produced is carried away by advection only, apart from the thermal boundary layer when it exists. In the bulk of the porous medium, we thus expect

$$\overline{w\theta}(z) = z. \tag{25}$$

As can be noticed in Figure 5, the advective heat flux is well described by the asymptotic law (25) even at Rayleigh numbers as low as $Ra = 29$. For BC 1, this agreement breaks down near the upper boundary where $\theta = 0$: The advection flux in the bulk is converted into a conductive heat flux over a boundary layer of depth $\mathcal{O}(Ra^{-1})$ which follows from Equation 23.

4.3.3. Nusselt Number

It is interesting to assess how efficient the convecting system is at transporting heat relative to purely diffusive transport. This is quantified by a Nusselt number N that provides a comparison between the total heat flux (including advective and diffusive contributions) and the diffusive heat flux (see, e.g., Goluskin, 2016),

$$N(t) \equiv \frac{\langle w\theta - Ra^{-1}\partial_z\theta\rangle}{-Ra^{-1}\langle\partial_z\theta\rangle} = \frac{Ra}{2\Delta\theta}, \tag{26}$$

$\langle\cdot\rangle$ denoting volume average, and where we have used that $\langle w\theta - Ra^{-1}\partial_z\theta\rangle = \langle z\rangle = 1/2$ and $\langle\partial_z\theta\rangle = \Delta\theta$ from (23) and (24). We define the mean Nusselt number Nu to be the long-time average of $N(t)$. Note that we retrieve that the transport is purely diffusive at threshold, since, at $Ra = Ra_c$, $\Delta\theta = Ra/2$ so that $Nu = 1$.

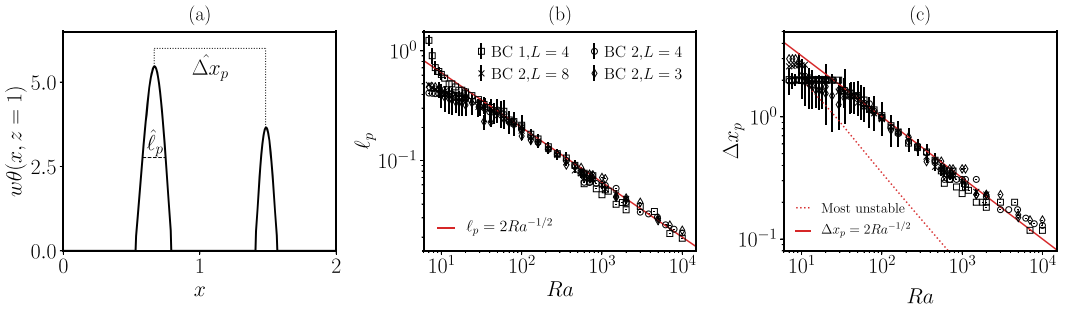

Figure 6. (a) vertical advective heat flux at the top boundary for Ra=200 with boundary condition BC 2 and aspect ratio L=4. The plot focuses on two plumes and shows graphically the definition of the plume separation $\Delta\hat{x}_p$ and the plume width $\hat{\ell}_p$. (b, c) Mean plume size ℓ_p and plume separation Δx_p, respectively, for all simulations with both boundary conditions BC 1 and BC 2. Both quantities scale with the Rayleigh number as $Ra^{-1/2}$. The error bars are determined by the standard deviation of the mean plume width and separation over a numerical run. The red dashed line indicates the plume separation for the most unstable mode, which follows a $Ra^{-3/4}$ power law.

Because $\Delta\theta = \mathcal{O}(1)$, we predict that, in the high Rayleigh number regime, $Nu \propto Ra$. For both boundary conditions BC 1 and 2, our simulations confirm this scaling down to $Ra \sim 20$ (see Figure 5b). There is a slight enhancement of the efficiency of heat transport as steady states emerge in the nonlinear regime of the instability around $Ra \sim 500$. The same scaling between Nu and Ra is also found in the classical Rayleigh-Bénard setup in a porous medium (Hewitt et al., 2012, 2014; Otero et al., 2004).

4.4. Plume Scales

In section 4.2, we observed that as the Rayleigh number Ra is increased, the typical width of the plumes and their typical spacing decreases. We obtain a quantitative measure of the mean plume size ℓ_p and separation Δx_p as a function of the Rayleigh number from the heat flux at the upper boundary. As shown in Figure 6a, plumes produce a series of heat-flux peaks. At each time step, we record the mean plume width $\hat{\ell}_p$ and plume separation distance $\Delta\hat{x}_p(t)$ over all plumes, and we define ℓ_p and Δx_p to be their long-time averages. Typical variability is given by the standard deviation of $\hat{\ell}_p$ and $\Delta\hat{x}_p$ over time. The result of this process is shown in Figures 6b and 6c: both the plume width and separation exhibit the same scaling with the Rayleigh number,

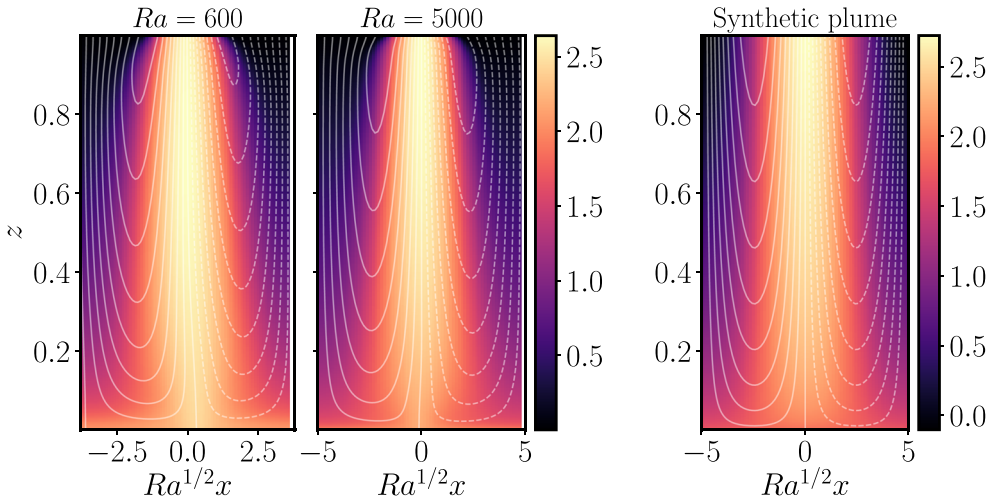

Figure 7. (left) Single plume isolated in the regime where the flow is steady and periodic in x, with boundary condition BC 1. (right) Synthetic field for a single plume obtained from the solution (38). The rescaled wave number $\tilde{k}$ is chosen to match the Ra=5,000 case, and its value is around 0.64. The integration constant θ_0 is chosen around 1.8 to roughly match the bottom temperature profiles observed in Figure 4. Note that although the streamlines do not seem to be vertical at the top boundary, a zoom shows that they ultimately bend to match verticality very close to the top boundary.

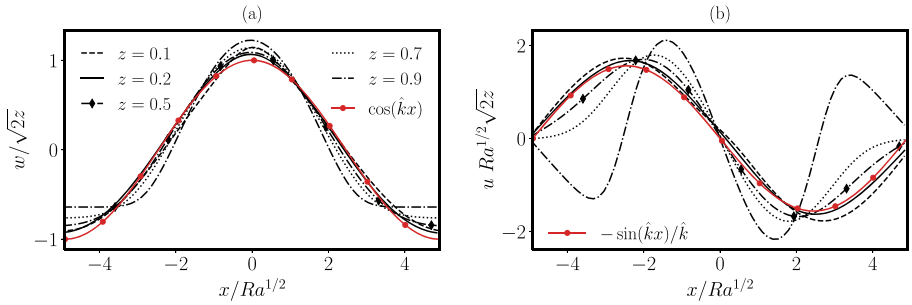

Figure 8. Horizontal profiles at different heights z of the scaled vertical (a) and horizontal (b) velocity across a plume. The amplitudes are normalized accordingly to the nonlinear solution (38). The expected structure is shown in red, and the only fitting parameter is the rescaled wave number $\hat{k} \simeq 0.64$. The Rayleigh number is $Ra = 5{,}000$, and the top boundary condition is BC 2.

that is $\ell_p, \Delta x_p \propto Ra^{-1/2}$, even close to the threshold. This power law cannot be explained by linear theory, even at low Ra, as the mean separation between plumes does not coincide with the most unstable mode predicted by the linear stability analysis (see Figure 6c). Instead, the typical scale of the plume is controlled by a balance between vertical advection, horizontal diffusion and heat production in (14), that is,

$$w\partial_z\theta \sim Ra^{-1}\partial_{xx}\theta \sim 1. \tag{27}$$

Given that temperature contrast remains $O(1)$, this balance demands both that the vertical velocity of the plume is $O(1)$ and that the typical lateral scale of the plume must be proportional to $Ra^{-1/2}$.

4.5. Asymptotic Plume Solution

Building on the scalings governing the typical plume size found numerically and theoretically, we derive here fully nonlinear solutions of the Equations 14 in the asymptotic limit $Ra \to \infty$. As explained below, the derivation of these equations allows us to confirm the balance at play in the plume formation.

In the bulk of the porous medium, since the gradients are $O(Ra^{1/2})$ in the x direction and $O(1)$ in the z direction, the incompressibility condition $\partial_x u + \partial_z w$ imposes a scaling on the ratio between u and w, that is $u/w = O(Ra^{-1/2})$. We thus introduce rescaled variables $\hat{x}$ and $\hat{u}$ such that

$$x = Ra^{1/2}\hat{x} \quad \text{and} \quad u = Ra^{-1/2}\hat{u}. \tag{28}$$

With these rescaled variables, the incompressibility condition is

$$\partial_{\hat{x}}\hat{u} + \partial_z w = 0. \tag{29}$$

Taking the curl of Darcy's law in (14) yields

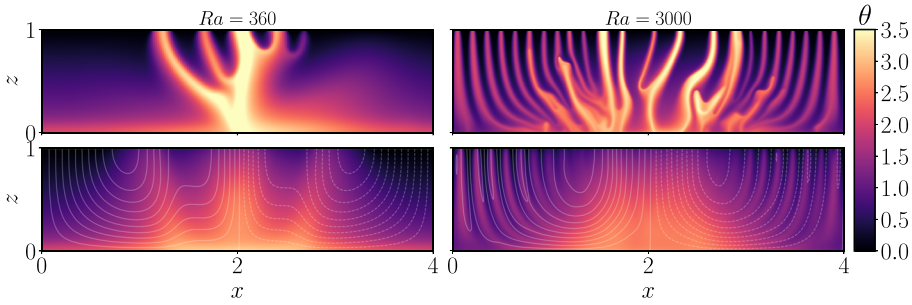

Figure 9. Snapshot of the temperature field for the heterogeneous heating case (top) and the time-averaged temperature and flow streamlines averaged (bottom).

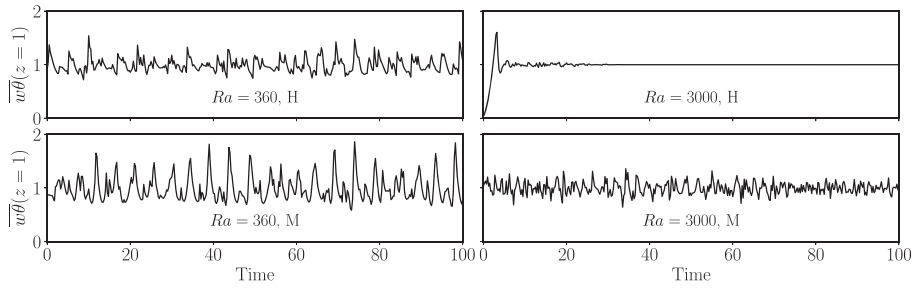

Figure 10. Horizontally averaged advective heat flux at the top boundary at Ra=360 (left) and Ra=3,000 (right), with comparison between homogeneous (top, H) and heterogeneous (bottom, M).

$$\partial_{\hat{x}} w = \partial_{\hat{x}} \theta + O(Ra^{-1}). \tag{30}$$

Hence, to leading order in Ra, $\theta - w$ is a function of z only. Because $\overline{w} = 0$, we infer that $\theta(\hat{x}, z) = w(\hat{x}, z) + \overline{\theta}(z)$. Thus, Darcy's law compels the temperature and the vertical velocity to have the same horizontal variance. Lastly, the advection-diffusion equation in (14) with rescaled variables is

$$\partial_t \theta + \hat{u}\partial_{\hat{x}}\theta + w\partial_z \theta = \partial_{\hat{x}\hat{x}}\theta + 1, \tag{31}$$

where all terms appear to be of the same order.

Building on our numerical results, we seek steady solutions that are periodic in the x direction. We introduce an ansatz for the flow that is the lowest order truncation of a Fourier series; that is, we assume the velocity field to have the following form,

$$\begin{cases} w &= w_0(z)\cos(\hat{k}\hat{x}) \\ \hat{u} &= \hat{u}_0(z)\sin(\hat{k}\hat{x}) \end{cases}, \tag{32}$$

which has no mean volume flux in either vertical or horizontal direction. According to the rescaled Darcy's law (30), the temperature becomes

$$\theta = w + \overline{\theta}(z) = w_0(z)\cos(\hat{k}\hat{x}) + \overline{\theta}(z). \tag{33}$$

For the flow (32) to satisfy the incompressibility condition, the following relation is required:

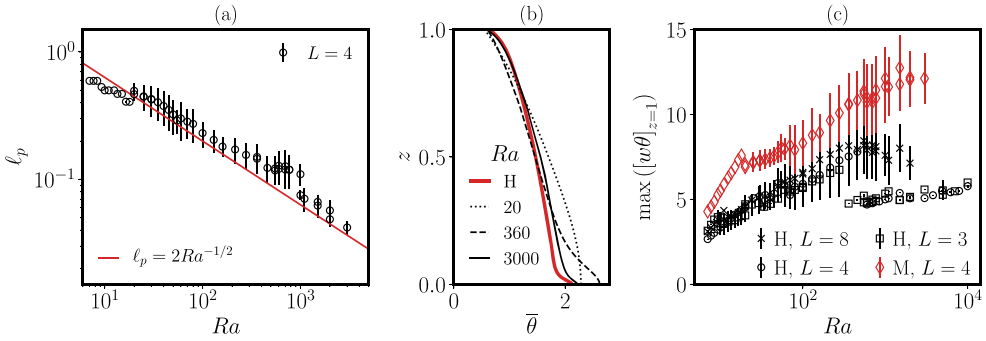

Figure 11. (a) Typical plume size in the heterogeneous heating case and comparison with the same law $\ell_p \propto Ra^{-1/2}$ as in Figure 6. The error bars are determined in the same way as in Figure 6. (b) Mean temperature profile for heterogeneous heating at several Rayleigh numbers; the red line corresponds to the temperature profile in the homogeneous case in the high Ra regime. (c) Maximum value of the nondimensional advective heat flux at the top of the porous layer determined from the simulations with BC 2. The error bar accounts for the standard deviation of the maximum value over the course of a simulation. Both homogeneous (Δq=0, labeled H) and heterogeneous (Δq=0.5, labeled M) are shown.

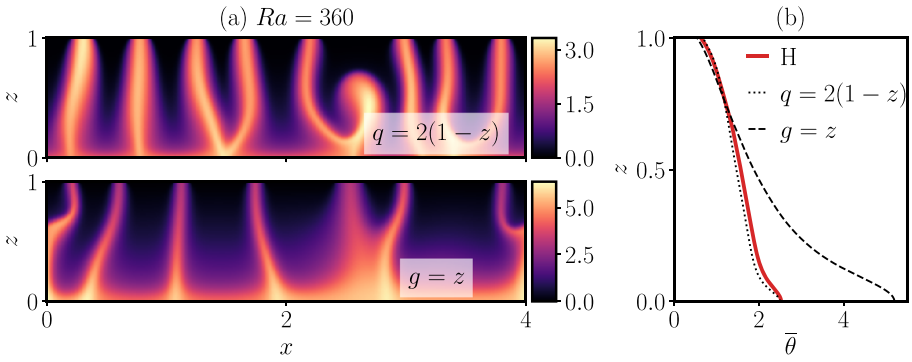

Figure 12. (a) Snapshots of the temperature field taken in the statistically steady state of simulations with Ra=360. In the upper one, the dimensionless heat production rate is a decreasing function of height q=2(1−z), whereas in the lower one, the dimensionless gravity is a linear function of height g=2z. (b) Superposition of the average temperature profiles at Ra=360 for the homogeneous heating (H), height-dependent heating, and height-dependent gravity cases.

$$w_0^{'} = -\hat{k}\hat{u}_0. \tag{34}$$

To determine the functions w_0 and $\overline{\theta}$, we use the advection-diffusion equation (31) which becomes

$$w_0 w_0^{'} \frac{1-\cos(2\hat{k}\hat{x})}{2} + w_0 w_0^{'} \frac{1+\cos(2\hat{k}\hat{x})}{2} + w_0 \overline{\theta}^{'} \cos(\hat{k}\hat{x}) = -\hat{k}^2 w_0 \cos(\hat{k}\hat{x}) + 1, \tag{35}$$

where the incompressibility condition (34) and Darcy's law (30) have been used. This equation contains mean and $\hat{k}$ harmonic terms that must be balanced, respectively. The mean terms simply yield a balance between vertical heat advection and heat production,

$$\frac{\mathrm{d}w_0^2}{\mathrm{d}z} = 2 \quad \text{that is,} w_0 = \sqrt{2z}. \tag{36}$$

The harmonic $\hat{k}$ terms correspond to a balance between horizontal diffusion and the vertical advection of the average thermal energy (or temperature) profile,

$$w_0 \overline{\theta}^{'} = -\hat{k}^2 w_0 \quad \text{that is,} \overline{\theta}(z) = \theta_0 - \hat{k}^2 z. \tag{37}$$

Table 2
A Summary of the Bulk Physical Parameters Used to Transpose Our Idealized Study to the Case of Enceladus' Core, Adapted From (Choblet et al., 2017)

Parameters	Values
Core radius (h)	186 km
Water density (ρ_0)	1.0×10^3 kg·m^{-3}
Matrix density (ρ_m)	2.8×10^3 kg·m^{-3}
Water heat capacity (c_0)	4.1×10^3 J·K^{-1}.kg^{-1}
Matrix heat capacity (c_m)	1.0×10^3 J·K^{-1}·kg^{-1}
Water conductivity (λ_0)	0.6×10^3 W·K^{-1}·m^{-1}
Matrix conductivity (λ_m)	2.8×10^3 W·K^{-1}·m^{-1}
Water thermal expansion (α)	1.2×10^{-3} K^{-1}
Kinematic viscosity (ν)	1×10^{-6} m^2·s^{-2}
Thermal diffusivity (κ)	6×10^{-7} m^2·s^{-2}
Porosity (ϕ)	0.20
Gravity (g)	0.1 m·s^{-2}

Note. See in particular the Supplementary Material of Choblet et al. (2017). Note that the modified porosity is $\overline{\phi} = 0.76$.

As noted in the preceding section, such a balance is responsible for setting the $O(Ra^{1/2})$ horizontal gradients.

We have, therefore, constructed a fully nonlinear solution that is exact in the asymptotic limit $Ra \to \infty$, and is given by

$$\begin{cases} u = -\dfrac{Ra^{-1/2}}{\hat{k}\sqrt{2z}} \sin(Ra^{1/2}\hat{k}x) \\ w = \sqrt{2z}\cos(Ra^{1/2}\hat{k}x) \\ \theta = \theta_0 - \hat{k}^2 z + \sqrt{2z}\cos(Ra^{1/2}\hat{k}x) \end{cases}, \tag{38}$$

where $\hat{k}$ and θ_0 are $O(1)$ but a priori unknown. Note that this solution only satisfies one boundary condition: the absence of volume flux at the bottom of the porous layer. The remaining boundary conditions, be it the absence of bottom heat flux, the purely vertical velocity at the top, or either of the thermal boundary condition BC 1 or BC 2, are all unmatched with the solution.

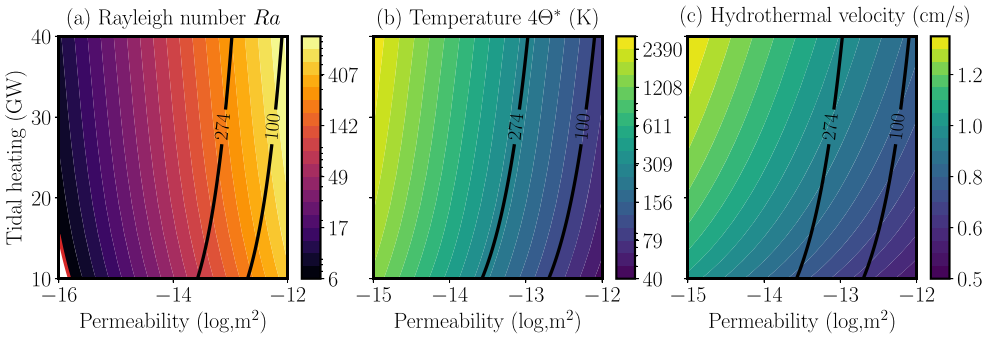

Figure 13. (a) the Rayleigh number as a function of the permeability and the tidal heating. The red line marks the onset of convection for the homogeneous heating case. (b) Typical maximum dimensional temperature $4\Theta^*$ (in Kelvin) (see (42)) inside the porous core of Enceladus. (c) Typical hydrothermal velocity obtained from the buoyancy flux at the bottom of the ocean as a function of permeability and tidal heating. On each panel, the 274 K isotherm gives the liquid-vapor transition at the hydrostatic pressure of core-ocean boundary, which represents a rough upper bound on the temperature for the model to remain valid with respect to phase change. The 100 K isotherm gives an estimate of the maximum temperature derived from geochemical measurements (Sekine et al., 2015; Hsu et al., 2015).

Figure 7 provides a comparison between plumes extracted from the simulations at two different Rayleigh numbers with a synthetic plume corresponding to the solution (38). The overall qualitative behavior of the two fields are the same, although the theoretical solution does not capture the shrinking of the plumes close the the top boundary, because it does not satisfy the boundary condition there.

To draw a more quantitative comparison between the nonlinear solution and the flow in one plume, we plot in Figure 8 several horizontal cuts at different heights of the vertical and horizontal velocities. We find that in the bulk, the theoretical solution adequately describes the amplitude of the velocity variations. However, the model becomes inaccurate near the upper boundary where, as noted above, it does not satisfy the correct boundary conditions. In fact, this issue seems to lead to other inaccuracies in the model: It predicts a linear decrease in the mean temperature $\overline{\theta}$, whereas the numerical simulations show a more complex dependence on z (Figure 4).

4.6. Conclusion for Nonlinear Heat Transport

Throughout this section, we have detailed the properties of heat transport by convection in strongly nonlinear regimes. Based on several arguments, including temperature scale, heat flux and Nusselt number measurement, we have confirmed that heat transport is dominated by advection in the bulk of the porous medium. We have carried out simulations with two different top boundary conditions that are thought to be relevant to geophysical context: one where the top boundary temperature is imposed and another where advective heat flux is conserved in upwellings and temperature is imposed in downwellings. We have confirmed that the two boundary conditions produce the same bulk flows. Lastly, we have shown that the typical plume size follows a $Ra^{-1/2}$ power law, which is due to a balance between horizontal diffusion and vertical advection of heat. It is interesting to note that internally heated and Rayleigh-Bénard convection are different regarding the typical plume scale: in the asymptotic regimes of large Ra, Hewitt et al. (2012) found that ℓ_p scaled like $Ra^{-0.4}$, which they later suggested was a result of the stability of the plumes (Hewitt & Lister, 2017).

5. Accounting for the Large-Scale Modulation of Tidal Heating

5.1. A Simple Model

In this section, we briefly explore how the large-scale variations of tidal heating affect heat transport in internally heated porous media. This is important for the case of icy satellites such as Enceladus, for which heterogeneity of tidal heating have been shown to induce focusing of the heat flux where heating is the most intense (Choblet et al., 2017). We consider here a domain with aspect ratio L=4 for which the volume production of heat q takes the form

$$q(x) = 1 - \Delta q \cos\left(\frac{2\pi}{L}x\right), \tag{39}$$

which is such that the mean heat production is unchanged compared the homogeneous case and the maximum heat production is located at the center of the domain. In the following, we only illustrate heat modulation with Δq=0.5 in the case of the boundary condition BC 2. Δq=0.5 is a good proxy for tidal heating which bears latitudinal and longitudinal variations by about a factor 2 between minima and maxima.

5.2. Large-Scale Flow and Pulsatility

The large-scale modulation of internal heating leads to the emergence of several striking features. The first one is the attraction of plumes toward the center where the heating is the most intense. Although plumes may exist in the whole interior of the domain, they merge toward the center, which results in a higher temperature region with larger heat flux anomaly, as illustrated in Figure 9. Plume merging toward the center is associated with a large-scale mean flow that is also shown in Figure 9. Note that at high Rayleigh number (Ra=3,000 in the snapshot of Figure 9), small-scale plumes persist in the time-averaged flow. Despite strong variability where heat production is maximal, some plumes remain locked in the areas where heat production is minimal, a feature that is reminiscent of the steady plumes of the homogeneous case.

Advection of the plumes toward the largest internal heating region and the subsequent plume merging leads to pulsatility in the advective heat flux, as shown in Figure 10. At intermediate Rayleigh number (Ra=360), the flux is intermittent for homogeneous heating but it exhibits a quasiperiodic behavior for a modulated heating. The typical period is of order 1; that is, it takes place over a convective time scale, and corresponds to the time needed for plume formation, advection toward the center and merging. The effects of heterogeneous heating are even more striking at high Ra: the steady state observed in the homogeneous case is replaced by quick oscillations of the heat flux (see Figure 10). They are due to the many plumes observed in the center of the domain reaching the top boundary non synchronously (see Figure 9).

5.3. Similarities With the Homogeneous-Heating Case

Despite the existence of a mean flow and the pulsatile behavior detailed in the preceding section, convection with heterogeneous internal heating bears many similarities with the homogeneous case. As already noticed earlier, small-cale plumes are still present in the flow, and their typical width remains proportional to $Ra^{-1/2}$ (see Figure 11) but with increased temporal and spatial variability. This means that the balance between horizontal diffusion, heat production, and vertical advection is still at play to determine the single plume dynamics.

Moreover, even if lateral variations of the mean temperature are obvious in Figure 9, the horizontally averaged temperature follows a trend that is very close to the homogeneous case, as shown in Figure 11. This observation suggests that the spatial form of heating is not particularly important for the mean dynamics and scaling laws governing heat transport in an internally heated porous medium.

5.4. Hydrothermal Velocity Driven in the Ocean

To conclude this theoretical analysis of internally heated porous convection, we derive a scaling law for the hydrothermal velocity driven by the hot plumes in the porous medium as they cross the upper boundary into the ocean above. To evaluate the typical velocity of the buoyant hot water coming out of the core at the bottom of the ocean, we must first determine the buoyancy flux associated with the porous plumes. The first question that arises concerns the transposition of the plumes observed in the present model to a three-dimensional geometry, as upwellings may take the form of isolated plumes or ascending sheets. Although there is no clear theoretical argument in favor of one or the other, several studies point toward the formation of sheets. Monnereau and Dubuffet (2002) have shown in viscous convection that the opening of the top boundary leads to a transition from plumes to sheets. In porous flows, sheet-like convection is observed in simulations of hydrothermal flows (Rabinowicz et al., 1998), and, in particular, in the model of Choblet et al. (2017) for the core of Enceladus. Therefore, we assume in the following that upwelling in the porous medium takes the form of sheets. As in the two-dimensional case, their typical extent is $Ra^{-1/2}$ because it remains set by the balance between vertical advection, horizontal diffusion and heat production given in Equation 27. At the bottom of the ocean, the sheets produce a line source of buoyancy flux B which

drives hydrothermal velocities U_h of order $B^{1/3}$. (Morton et al., 1956; Woods, 2010). The dimensional buoyancy flux is given by (Woods, 2010)

$$B = \int_{\text{upwelling}} \alpha g (\Theta W)|_{z=h} \, \mathrm{d}x, \tag{40}$$

where the one-dimensional integral is computed across an upwelling zone of typical extent $\ell_p \propto Ra^{-1/2}$. As Θ and W are proportional to Ra, B scales like $Ra^{3/2}$, or more explicitly,

$$B \simeq \frac{\kappa^2 \nu}{kh} Ra^{3/2} \, (w\theta)|_{z=h} \quad \text{and} \quad U_h = \left(\frac{\kappa^2 \nu}{kh} (w\theta)|_{z=h} \right)^{1/3} Ra^{1/2}, \tag{41}$$

where we have used the velocity and temperature scales defined in Equation 12. Focusing of the heat flux in narrow upwelling zones leads to enhanced values of $(w\theta)|_{z=h}$, as shown in Figure 11c. In the case of heterogeneous heating, focusing increases the heat flux at the bottom of the ocean by about a factor of 10 over the range of Rayleigh numbers considered here.

6. Application of the Idealized Study to the Case of Enceladus

6.1. From a Two-Dimensional Model to a Planetary Core

To carry out our idealized study of internally heated porous convection, we have discarded many ingredients that will be important for Enceladus, as stated prior to the introduction of the model (section 2.1). Before applying our results, we review these approximations and evaluate how they may affect the conclusions drawn from the two-dimensional Cartesian model.

6.1.1. Sphericity

First, the definition of the velocity, temperature and time scales as well as the Rayleigh number defined in section 2.3 rely entirely on dimensional analysis and are thus insensitive to the geometry. The dimensionless Equations (14) thus take the same expression in any geometry. The critical Rayleigh number above which convection takes place will, presumably, be modified by the geometry, although Choblet et al. (2017) found convective flows down to $Ra \simeq 8$ in simulations in a spherical geometry, which puts an upper bound on Ra_c that is similar to what we find in a Cartesian geometry.

We expect that the typical size of upwellings will retain a $Ra^{-1/2}$ scaling in spherical geometry, because the balance in (27) that gives this scaling remains the same: lateral second derivatives must be of order Ra for orthoradial diffusion to be in balance with heat production and radial advection. As a consequence, our prediction for the typical buoyancy flux and hydrothermal-velocity scales should still hold in a spherical geometry.

Nevertheless, there will inevitably be differences between the flow in a Cartesian and spherical geometry. For example, the ratio of surface area to volume is different, which affects the energy conservation equation for the time-averaged radial heat flux $\nabla \cdot (\overline{J}(r)\boldsymbol{e}_r) = 1$ (cf. Equation 24). This constraint imposes $\overline{J}(r) = r/3$, and the volume-averaged heat flux becomes $\langle J \rangle = 1/6$, which is a factor of 3 smaller than in a Cartesian geometry. As a consequence, we expect heat flux anomalies to either have lower amplitudes or be sparser. This simple analysis suggests that the Cartesian geometry might give an upper bound on the buoyancy flux and the hydrothermal velocity induced in the ocean compared to the real spherical case.

6.1.2. Depth Dependence of Heat Production and Gravity

The model developed here also neglects any vertical variations of gravity and volumetric heat production, and we briefly explore their possible importance here with the aid of a few additional simulations. Volumetric heat production on Enceladus decreases away from the center to become negligible close to the surface (Choblet et al., 2017), although the decreases remains sufficiently slow for the heat production averaged over the spherical shell to increase with radius. In the uniform heating case, we have found that the structure of the flow is governed by a local balance between advection, diffusion and volumetric heat production. We anticipate such a balance to remain at play when heat production varies with depth which makes the volumetric heating variations more relevant to the dynamics than those of the shell-averaged heating. Therefore, to test the effect of vertical variations of heat production, we have carried out simulations with a decreasing source term $q(z)=2(1-z)$ in the advection-diffusion equation that retains the same spatial

average as in the uniform case. A typical snapshot is shown in Figure 12 along with the mean vertical temperature profile, $\overline{\theta}$. They both show very little difference from the uniform-heating case (see Figure 3), suggesting that vertical variation in heat production does not play an important dynamical role, at least in Cartesian geometry.

The picture is slightly changed when we consider uniform heating but with a depth-dependent gravitational field. In a uniform-density planetary core, we expect g to increase linearly with radius, and so we carried out a few example simulations in which the dimensionless gravity is $g{=}z$ (i.e., gravity is normalized by its surface value). The effect of this on the equations is to add a factor z in front of the temperature in the dimensionless version of Darcy's law (see Equations 14). A snapshot of the temperature field (Figure 12) reveals that plumes are narrower and less numerous than in the homogeneous case. As a consequence, the maximum advective flux carried by the plumes is roughly double that of the homogeneous case. The average temperature profile is also strikingly different: Weaker gravity at depth makes advection inefficient as a means of evacuating heat, resulting in larger temperature at the bottom of the domain. However, because plumes are thinner, lateral diffusion is enhanced and the plume temperature decreases as they rise. As a consequence, the hot spot temperature at the upper surface remains similar to the modulated case, that is, $\max(\theta(z{=}1)){\sim}4$.

Note that the variations with z of gravity and heat production do not affect the scaling $Ra^{-1/2}$ governing the size of the plumes (and hence the hydrothermal velocity). Since the dimensionless gravity and volumetric heating remain at most order 1, the balance between horizontal diffusion, heat production and vertical advection still holds in the same way as in the uniform case. In fact, the asymptotic expansion of section 4.5 can be reworked with z-dependent gravity and volumetric heating down to Equation 31 without affecting the hierarchy between each term. Therefore, the scaling laws we have derived in the preceding sections are robust to these additional physical ingredients.

We also briefly considered the effect of depth dependence in the modulation amplitude Δq for the results presented in section 5, since the modulation should increase with depth, being almost negligible near the core (Choblet et al., 2017). We carried out simulations with $\Delta q{=}z$, which retains the same average modulation as previously. Results showed little change from those discussed in section 5: A mean flow drags small-scale plumes toward the areas with larger volumetric heating which causes the flow to be unsteady. The strong pulsatility with bursts of heat flux observed at $Ra{=}360$ in Figure 10 are weaker, however, with the time series of $\overline{w\theta}(z=1)$ being more similar to the homogeneous case.

6.2. Quantification of Convection in Enceladus' Core

The preceding discussion suggests that the simplified two-dimensional Cartesian model of internally heated porous convection produces scaling laws that provide a reasonable description of the flow and the hydrothermal activity inside icy moons, at least in terms of orders of magnitude. Here we apply our results to Enceladus.

6.2.1. Physical Properties of Enceladus' Core

To characterize convection inside Enceladus' core and to compare our results to existing literature, we use the same physical parameters as in Choblet et al. (2017). A set of fixed physical constants that are relevant to characterize heat transport are given in Table 2. We reproduce the process used in Choblet et al. (2017) and do not precisely specify the permeability k and internal heat production Q_V values on which the uncertainty is the largest. Instead, we consider that k may range from 10^{-15} to 10^{-12} m^2 and that the tidal heating is between 10 and 40 GW. (The lower bound is directly inferred from the heat flux measurement at the south pole of Enceladus Spencer et al., 2006, 2018.) Therefore, we draw maps of the behavior of the system keeping the parameters of Table 2 constant and varying both k and Q_V.

6.2.2. The Rayleigh Number Inside Enceladus

As explained in section 2.3, the overall behavior of the system depends only on one dimensionless parameter, the Rayleigh number, defined in (13), which which is a power law of both k and Q_V. The map of the possible values of the Rayleigh number inside the core of Enceladus is given in Figure 13. In the range of values of k considered by Choblet et al. (2017), the system is always unstable to convection, although Ra does not reach very high values and remains below 1,000.

6.2.3. Maximum Temperature

We have shown in section 4.3 that heat transport is mostly advective, even at values of the Rayleigh number that are close to the onset of the instability.In such a regime, the dimensionless temperature takes $O(1)$ values, with a maximum of about 4 in the case of horizontally modulated heat production (see for instance the snapshots of Figure 9) that is reached at the core of the plumes.Hence, $4\Theta^*$ is a good proxy for the maximum temperature difference between the ocean and the core of Enceladus, with Θ^* the temperature scale defined in section 2.3,

$$\Theta^* = \frac{\kappa\nu}{k\alpha g h} Ra. \tag{42}$$

The maximum temperature difference $4\Theta^*$ is shown in Figure 13 and, depending on the parameters, it ranges from 40 to 3000 K.

The computation of the maximum temperature difference allows us to determine the limit of validity of our model which does not include phase change of water from liquid into vapor. On the one hand, according to the snapshots of Figures 3 and 9, the core temperature of plumes is almost constant with height. On the other hand, the boiling point of water is an increasing function of pressure and depth. As a consequence, the maximum temperature allowed in our model is given by the boiling point of water at the core-ocean boundary. Assuming that the core lies below 60 km of liquid and solid water with density 1×10^3 kg·m^{-3} and constant gravity, a crude estimate for the pressure is 6 MPa at the core-ocean boundary. The corresponding boiling point for pure water is 547 K (Haynes, 2012). If we assume the ocean to be well mixed and made of pure water, its averaged temperature should be similar to the fusion temperature of ice, that is, 273 K (Haynes, 2012). Hence, we show in Figure 13 the isotherm 274 K which gives a crude upper bound on the validity of the single-phase model that is used here and in the literature dealing with internal models of icy moons, although other additional ingredients (composition, variable gravity) may shift this upper bound in a way that remains to be determined.

Note that Hsu et al. (2015) have shown via the ice plume composition that the water flowing inside Enceladus has been in contact with rocks at a temperature of about 90°C. We show in Figure 13 the location of where the maximum temperature difference reaches 100 K which roughly corresponds to this important constraint on the maximum temperature. Our idealized model suggests a constraint on the permeability of Enceladus' core of 10^{-13} to 10^{-12} m^2, for the range of tidal heating considered.

6.2.4. Hydrothermal Velocity in Enceladus' Ocean

Using the law (41) governing the buoyancy flux B driven by porous convection in the ocean, we compute the typical hydrothermal velocity $B^{1/3}$ in Enceladus' ocean. With dimensionless heat flux $w\theta\sim10$ in the core of the thermal anomalies, the typical hydrothermal velocity is found to be about 1 cm·s^{-1}, no matter what the permeability or the tidal heating are (see Figure 13c). This value is in agreement with the typical velocity found by Choblet et al. (2017) with different scaling arguments relying on the power anomaly advected to the ocean floor. As a consequence, for a subsurface ocean whose thickness is of the order 10–30 km (Thomas et al., 2016), the expected turnover timescale is of the order of a month, at most.

6.2.5. Typical Velocity and Temporal Variability

The typical velocity scale U^* of the flow in the core is given by a diffusive velocity κ/h augmented by a factor Ra, that is,

$$U^* = \frac{\kappa}{h} Ra. \tag{43}$$

The diffusive velocity scale amounts to 0.1 mm·yr^{-1}, and because Ra does not exceed 10^3, the Darcy flux remains below 10 cm·yr^{-1}. The hydrothermal activity at the bottom of Enceladus' ocean is therefore very different from the what is commonly observed at the bottom of the Earth's oceans, where typical Darcy fluxes are rather of the order of a few meters per year (10^3 times larger). This difference is largely due to the much weaker gravitational acceleration in Enceladus.

Consequently, the convective time scale τ is

$$\tau = \overline{\varphi}\frac{h}{U^*} = \overline{\varphi}\frac{h^2}{\kappa}Ra^{-1} \simeq 0.8 \text{ Gy} \times Ra^{-1}. \quad (44)$$

The typical variability timescale, for instance for the flux at the top boundary (see Figure 10) is thus at least 1 Myr. It is a very slowly evolving system compared to the turnover timescale of the subsurface ocean, or to the timescale of human observations. In our simulations, we have observed bursts in the convective activity that give rise to a 40–50% increase in the average heat flux at the surface of the core that may last for a few million years. These bursts correspond to more active plumes that would cause enhanced hydrothermal activity inducing preferential erosion of the ice shell above. One may thus speculate that, in the past, intense plumes similar to the one at the south pole of Enceladus could have been active at other locations. Such a hypothesis might explain the existence of older tectonized terrains at the surface of Enceladus (Crow-Willard & Pappalardo, 2015). Lastly, localized bursts could also be at the start of the runaway mechanism proposed by Choblet et al. (2017) to explain the asymmetry between the north and south poles of Enceladus: A thinner ice crust locally enhances tidal heating, which in turn enhances ice erosion.

7. Conclusion and Discussion

Throughout this article, we have explored heat transport in a fluid-saturated, internally heated porous medium with an idealized Cartesian model. Our setup is based on an idealization of the model of Choblet et al. (2017) describing the tidally driven hydrothermal activity in the interior of Enceladus. The behavior of the system is governed by a single dimensionless number, the Rayleigh number Ra, which is an increasing function of both the permeability and the internal heat production. With the combination of numerical simulations and mathematical analysis, we have derived general laws governing hydrothermal activity driven by volumetric heating.

We have shown that heat transport in the porous medium is governed by advection. In this regime, the temperature difference between the porous matrix and the pure fluid ocean scales like Ra. This scaling enables use to constrain the plausible range of values for the permeability of Enceladus' core. According to Hsu et al. (2015), the temperature scale should be at most 100 K. For values of tidal heating that are consistent with the heat flux measurement at the surface of Enceladus, our scaling indicates that the permeability should be around 10^{-13}–10^{-12} m^2.

In our simulations, we have reproduced the observation drawn from the simulations of Choblet et al. (2017) that the upwelling zones tend to narrow as the Rayleigh number is increased, and that they concentrate where internal heating is the most intense. Our simulations show that the typical plume size follows a $Ra^{-1/2}$ power law, which is imposed by a balance between vertical advection and horizontal diffusion of heat. This law governing the size of heat-flux anomalies at the bottom of the ocean of Enceladus compels the typical buoyancy flux injected into the ocean to be proportional to $Ra^{3/2}$. Over the range of tidal heating and permeability that are consistent with observational data, we have found that the typical hydrothermal velocity in the ocean of Enceladus is about 1 cm·s^{-1}. Despite the idealization of our model, such an estimate is consistent with the one derived by Choblet et al. (2017) from an estimate of a typical heat flux anomaly. The model used here has also helped us to highlight the underpinning of heat transport in an internally heated porous layers. In particular, we have shown that the heat transport efficiency, which has been characterized via a generalized Nusselt number, has the same scaling as the classical Rayleigh-Bénard convection in porous media (Hewitt et al., 2012, 2014; Otero et al., 2004).

Despite the highly idealized nature of our approach, we have argued that the scaling laws found for the typical size of thermal anomalies, the time variability, and the hydrothermal activity are also expected in spherical geometry and are robust to the inclusion of additional ingredients such as vertical variations of heat production and gravity. These scaling laws could thus be applied to the other small icy moons of the Solar System, in particular those of Saturn's E ring, whose internal structure is similar to Enceladus' (Nimmo & Pappalardo, 2016). Although Enceladus is the only one showing signs of present internal activity, these other bodies could have been active in the past. Our study thus paves the way for more systematic understanding of the thermal evolution of these bodies. It could also apply to larger icy moons such as Europa where the ocean is in contact with a rocky mantle that is internally heated by radiogenic decay.

Of course, the simple scaling arguments contained here are not a substitute for a detailed investigation of the idealized problem in a spherical geometry, which would be a useful future extension to this work. Such a study would give a clearer picture of the flow structures in a spherical geometry, as well providing more quantitative predictions of hot spot widths, time variability and strength. Beyond these geometrical considerations, there are also other effects that have not been discussed here or in the existing literature that could lead to significant changes in convective heat transport. One major simplification of all models of porous planetary interiors is the assumption of homogeneous and isotropic permeability k. Since the core of small icy satellites such as Enceladus' is an aggregate of heterogeneous material, their permeability is unlikely to be uniform. It is not even clear whether coarse-grained modeling based on the assumption of strong confinement, that is, Darcy's law, is entirely relevant for the core of icy satellites, although, as we have seen, Darcy's law with small permeability is consistent with observed data. However, we do not believe any significant progress can be achieved in these directions without further constraining the core's small-scale structure.

In addition, the model we consider completely discards flows that are directly driven by the periodic tidal distortion. Although the tidal deformation field is purely incompressible in continuous media, mean flows analogous to Stokes drift may result from the periodic motion of the porous matrix. Whether deformation-driven flows are comparable to buoyancy-driven flows remains to be quantified.

Lastly, there is a need to clarify the behavior of the system at the top of the porous core and the coupling between the porous layer and the above ocean. We have stated in the second section that the two possible thermal boundary conditions used here (imposed temperature or free temperature in the upwellings) are the two end-members of the behavior of the fluid at the interface. The imposed-temperature condition could represent a very slow porous layer lying underneath a very well-mixed ocean. This situation could be relevant to the case of Enceladus and other icy moons as the Darcy flux ($\sim 1\ \mathrm{cm{\cdot}yr^{-1}}$) is very small compared to the hydrothermal velocity ($\sim 1\ \mathrm{cm{\cdot}s^{-1}}$). In this configuration, the water coming out of the core is at the same temperature as the ocean and is neutrally buoyant; there is then no hydrothermal activity in the sense of what we know at the bottom of the Earth's ocean. Nevertheless, it is associated to a diffusive heat flux anomaly on the subsurface ocean's floor which is likely to drive convection and mixing in the ocean. The observed chemical signature of contact with silicate rocks at high temperature (Hsu et al., 2015) could very well happen below the thin thermal boundary layer at the top of the core. Moreover, current thermal evolution models of icy moons rely on parametrization of hydrothermally driven convection in the subsurface ocean that are based on the classical Rayleigh-Bénard problem (Travis & Schubert, 2015; Travis et al., 2012). It is, however, not clear at all whether such parametrization actually applies to the present system where ocean convection is driven by strong and localized heterogeneities of either the advective or the diffusive heat flux at the bottom boundary. In short, it remains difficult to produce a definitive statement about the thermal structure of the subsurface ocean without a careful study of the coupled system with two very different typical evolution timescales for each medium.

Data Availability Statement

The source codes and output data are available on Figshare (Le Reun & Hewitt, 2020).

Acknowledgments

The authors acknowledge support from the 2018 WHOI GFD program, supported by the U.S. National Science Foundation (Award 1332750) and the Office of Naval Research, where most of this research was carried out. T. L. R. is supported by the Royal Society through a Newton International Fellowship (Grant Reference NIF\R1\192181).

References

Buretta, R. J., & Berman, A. S. (1976). Convective heat transfer in a liquid saturated porous layer. *Journal of Applied Mechanics*, *43*(2), 249–253. https://doi.org/10.1115/1.3423818

Choblet, G., Tobie, G., Sotin, C., Běhounková, M., Čadek, O., Postberg, F., & Souček, O. (2017). Powering prolonged hydrothermal activity inside Enceladus. *Nature Astronomy*, *1*, 841–847. https://doi.org/10.1038/s41550-017-0289-8

Coumou, D., Driesner, T., & Heinrich, C. A. (2008). The structure and dynamics of mid-ocean ridge hydrothermal systems. *Science*, *321*(5897), 1825–1828. https://doi.org/10.1126/science.1159582

Coumou, D., Driesner, T., Weis, P., & Heinrich, C. A. (2009). Phase separation, brine formation, and salinity variation at Black Smoker hydrothermal systems. *Journal of Geophysical Research*, *114*, B03212. https://doi.org/10.1029/2008JB005764

Crow-Willard, E. N., & Pappalardo, R. T. (2015). Structural mapping of Enceladus and implications for formation of tectonized regions. *Journal of Geophysical Research: Planets*, *120*, 928–950. https://doi.org/10.1002/2015JE004818

Cserepes, L., & Lenkey, L. (2004). Forms of hydrothermal and hydraulic flow in a homogeneous unconfined aquifer. *Geophysical Journal International*, *158*(2), 785–797. https://doi.org/10.1111/j.1365-246X.2004.02182.x

Drazin, P. G. (2002). *Introduction to hydrodynamic stability*. Cambridge University Press.

Fontaine, F. J., & Wilcock, W. S. D. (2007). Two-dimensional numerical models of open-top hydrothermal convection at high Rayleigh and Nusselt numbers: Implications for mid-ocean ridge hydrothermal circulation: Hydrothermal convection. *Geochemistry, Geophysics, Geosystems*, *8*, Q07010. https://doi.org/10.1029/2007GC001601

Goluskin, D. (2016). A family of convective models. *Internally heated convection and Rayleigh-Bénard convection* (pp. 1–26). Springer, Cham. https://doi.org/10.1007/978-3-319-23941-5_1

Hardee, H. C., & Nilson, R. H. (1977). Natural convection in porous media with heat generation. *Nuclear Science and Engineering*, *63*(2), 119–132. https://doi.org/10.13182/NSE77-A27015

Haynes, W. M. (2012). *CRC handbook of chemistry and physics* (93rd). CRC Press.

Hewitt, D. R., & Lister, J. R. (2017). Stability of three-dimensional columnar convection in a porous medium. *Journal of Fluid Mechanics*, *829*, 89–111. https://doi.org/10.1017/jfm.2017.561

Hewitt, D. R., Neufeld, J. A., & Lister, J. R. (2012). Ultimate regime of high Rayleigh number convection in a porous medium. *Physical Review Letters*, *108*(22), 224503. https://doi.org/10.1103/PhysRevLett.108.224503

Hewitt, D. R., Neufeld, J. A., & Lister, J. R. (2014). High Rayleigh number convection in a porous medium containing a thin low-permeability layer. *Journal of Fluid Mechanics*, *756*, 844–869. https://doi.org/10.1017/jfm.2014.478

Hsu, H.-W., Postberg, F., Sekine, Y., Shibuya, T., Kempf, S., Horányi, M., et al. (2015). Ongoing hydrothermal activities within Enceladus. *Nature*, *519*(7542), 207–210. https://doi.org/10.1038/nature14262

Kulacki, F. A., & Ramchandani, R. (1975). Hydrodynamic instability in a porous layer saturated with a heat generating fluid. *Wärme- und Stoffübertragung*, *8*(3), 179–185. https://doi.org/10.1007/BF01681559

Lainey, V., Jacobson, R. A., Tajeddine, R., Cooper, N. J., Murray, C., Robert, V., et al. (2017). New constraints on Saturn's interior from Cassini astrometric data. *Icarus*, *281*, 286–296. https://doi.org/10.1016/j.icarus.2016.07.014

Le Reun, T., & Hewitt, D. R. (2020). Internally heated porous convection: An idealised model for Enceladus' hydrothermal activity. https://doi.org/10.6084/m9.figshare.11973591.v2

Monnereau, M., & Dubuffet, F. (2002). Is Io's mantle really molten? *Icarus*, *158*(2), 450–459. https://doi.org/10.1006/icar.2002.6868

Morton, B. R., Taylor, G. I., & Turner, J. S. (1956). Turbulent gravitational convection from maintained and instantaneous sources. *Proceedings of the Royal Society of London. Series A*, *234*(1196), 1–23. https://doi.org/10.1098/rspa.1956.0011

Nield, D. A., & Bejan, A. (2013). Heat transfer through a porous medium. In D. A. Nield & A. Bejan (Eds.), *Convection in porous media* (pp. 31–46). New York, NY: Springer. https://doi.org/10.1007/978-1-4614-5541-7_2

Nield, D. A., & Kuznetsov, A. V. (2013). Onset of convection with internal heating in a weakly heterogeneous porous medium. *Transport in Porous Media*, *98*(3), 543–552. https://doi.org/10.1007/s11242-013-0158-6

Nimmo, F., & Pappalardo, R. T. (2016). Ocean worlds in the outer solar system. *Journal of Geophysical Research: Planets*, *121*, 1378–1399. https://doi.org/10.1002/2016JE005081

Otero, J., Dontcheva, L. A., Johnston, H., Worthing, R. A., Kurganov, A., Petrova, G., & Doering, C. R. (2004). High-Rayleigh-number convection in a fluid-saturated porous layer. *Journal of Fluid Mechanics*, *500*, 263–281. https://doi.org/10.1017/S0022112003007298

Press, W. H., Teukolsky, S. A., Vetterling, W. T., & Flannery, B. P. (1992). *Numerical recipes in FORTRAN* (2nd). Cambridge [England] ; New York: Cambridge University Press.

Rabinowicz, M., Boulègues, J., & Genthon, P. (1998). Two- and three-dimensional modeling of hydrothermal convection in the sedimented Middle Valley segment, Juan de Fuca Ridge. *Journal of Geophysical Research*, *103*(B10), 24,045–24,065.

Roberts, J. H. (2015). The fluffy core of Enceladus. *Icarus*, *258*, 54–66. https://doi.org/10.1016/j.icarus.2015.05.033

Sekine, Y., Shibuya, T., Postberg, F., Hsu, H.-W., Suzuki, K., Masaki, Y., et al. (2015). High-temperature water–rock interactions and hydrothermal environments in the chondrite-like core of Enceladus. *Nature Communications*, *6*(1), 1–8. https://doi.org/10.1038/ncomms9604

Souček, O., Kalousová, K., & Čadek, O. (2014). Water transport in planetary ice shells by two-phase flow—A parametric study. *Geophysical & Astrophysical Fluid Dynamics*, *108*(6), 639–666. https://doi.org/10.1080/03091929.2014.969251

Spencer, J. R., Nimmo, F., Ingersoll, A. P., Hurford, T. A., Kite, E. S., Rhoden, A. R., et al. (2018). Plume origins and plumbing: From ocean to surface. In P. M. Schenk, R. N. Clark, C. J. A. Howett, A. J. Verbiscer, & J. H. Waite (Eds.), *Enceladus and the icy moons of Saturn* (pp. 163–174). Tucson, AZ: University of Arizona Press.

Spencer, J. R., Pearl, J. C., Segura, M., Flasar, F. M., Mamoutkine, A., Romani, P., et al. (2006). Cassini encounters Enceladus: Background and the discovery of a south polar hot spot. *Science*, *311*(5766), 1401–1405. https://doi.org/10.1126/science.1121661

Thomas, P. C., Tajeddine, R., Tiscareno, M. S., Burns, J. A., Joseph, J., Loredo, T. J., et al. (2016). Enceladus's measured physical libration requires a global subsurface ocean. *Icarus*, *264*, 37–47. https://doi.org/10.1016/j.icarus.2015.08.037

Travis, B. J., Palguta, J., & Schubert, G. (2012). A whole-moon thermal history model of Europa: Impact of hydrothermal circulation and salt transport. *Icarus*, *218*(2), 1006–1019. https://doi.org/10.1016/j.icarus.2012.02.008

Travis, B. J., & Schubert, G. (2015). Keeping Enceladus warm. *Icarus*, *250*, 32–42. https://doi.org/10.1016/j.icarus.2014.11.017

Woods, A. W. (2010). Turbulent plumes in nature. *Annual Review of Fluid Mechanics*, *42*(1), 391–412. https://doi.org/10.1146/annurev-fluid-121108-145430